

Roughness induced forced convective laminar-transitional micropipe flow: energy and exergy analysis

A. Alper Ozalp

Received: 7 June 2007 / Accepted: 21 April 2008 / Published online: 16 May 2008
© Springer-Verlag 2008

Abstract Variable fluid property continuity, Navier–Stokes and energy equations are solved for roughness induced forced convective laminar-transitional flow in a micropipe. Influences of Reynolds number, heat flux and surface roughness, on the momentum-energy transport mechanisms and second-law of thermodynamics, are investigated for the ranges of $Re = 1\text{--}2,000$, $Q = 5\text{--}100 \text{ W/m}^2$ and $\varepsilon = 1\text{--}50 \text{ }\mu\text{m}$. Numerical investigations put forward that surface roughness accelerates transition with flatter velocity profiles and increased intermittency values (γ); such that a high roughness of $\varepsilon = 50 \text{ }\mu\text{m}$ resulted in transitional character at $Re_{\text{tra}} = 450$ with $\gamma = 0.136$. Normalized friction coefficient (C_f^*) values showed augmentation with Re , as the evaluated C_f^* are 1.006, 1.028 and 1.088 for $Re = 100, 500$ and 1,500, respectively, at $\varepsilon = 1 \text{ }\mu\text{m}$, the corresponding values rise to $C_f^* = 1.021, 1.116$ and 1.350 at $\varepsilon = 50 \text{ }\mu\text{m}$. Heat transfer rates are also recorded to rise with Re and ε ; moreover the growing influence of ε on Nusselt number with Re is determined by the $Nu_{\varepsilon=50 \text{ }\mu\text{m}}/Nu_{\varepsilon=1 \text{ }\mu\text{m}}$ ratios of 1.086, 1.168 and 1.259 at $Re = 500, 1,000$ and 1,500. Thermal volumetric entropy generation ($\dot{S}_{\Delta T}'''$) values decrease with Re and ε in heating; however the contrary is recorded for frictional volumetric entropy generation ($\dot{S}_{\Delta P}'''$) data, where the augmentations in $\dot{S}_{\Delta P}'''$ are more considerable when compared with the decrease rates of $\dot{S}_{\Delta T}'''$.

List of symbols

a	curve fit constants
A	cross-sectional area (m^2)
C_d	discharge coefficient
C_f	friction coefficient
C_f^*	normalized friction coefficient
C_v	constant volume specific heat (J/kgK)
C_p	constant pressure specific heat (J/kgK)
D	diameter (m)
e	internal energy per unit mass (J/kg)
$f_\varepsilon(z)$	surface roughness model function
h	convective heat transfer coefficient ($\text{W/m}^2\text{K}$)
H	shape factor
k	kinetic energy per unit mass (J/kg)
L	pipe length (m)
\dot{m}	mass flow rate (kg/s)
M	Mach number
Nu	Nusselt number
P	static pressure (Pa)
Q	surface heat flux (W/m^2)
\dot{Q}	volumetric flow rate (m^3/s)
R	radius (m), gas constant (J/kgK)
Re	Reynolds number
S	total entropy generation (W/K)
S'''	total volumetric entropy generation ($\text{W/m}^3\text{K}$)
$S_{\Delta P}'''$	frictional volumetric entropy generation ($\text{W/m}^3\text{K}$)
$S_{\Delta T}'''$	thermal volumetric entropy generation ($\text{W/m}^3\text{K}$)
T	temperature (K)
U	axial velocity (m/s)
\vec{V}	velocity vector

A. A. Ozalp (✉)
Department of Mechanical Engineering,
University of Uludag,
16059 Gorukle, Bursa, Turkey
e-mail: aozalp@uludag.edu.tr

Greek symbols

α	thermal diffusivity (m^2/s)
ε	roughness amplitude (μm)
ε^*	non-dimensional surface roughness ($=\varepsilon/D$)

ϕ	irreversibility distribution ratio
κ_f	thermal conductivity of fluid (W/mK)
γ	intermittency
μ	dynamic viscosity (Pa s)
ρ	density (kg/m ³)
τ	shear stress (Pa)
ξ	air properties
ψ_{inp}	energy input (W)
ψ_{loss}	energy loss (W)
ω	roughness period (μm)
Ξ	entropy generation aspect ratio

Subscripts

c, s	center, surface
i	dimension
in	inlet
lam	laminar
m, o	maximum, mean
r, θ, z	radial, peripheral, axial
tra	transition
turb	turbulent

Superscripts

T	temperature dependency
–	volumetric average

1 Introduction

In various thermo-fluid systems, irreversibility is widely accepted as a general criterion for determining the amount of wasted useful energy, where the design studies, concentrating on internal flow, mainly focus on controlling the overall entropy generation. Flow and heat transfer characteristics are the main concerns of internal flow applications; however investigations on surface roughness based viscous effects, velocity and temperature profiles (TP) constitute a wide research area due to their direct role in entropy generation of thermo-fluid systems; and have recently been the topic of great interest in various fields such as fuel cells [1], heat exchangers [2] and even for micropipe systems [3].

In the last decade, momentum and heat transfer investigations of laminar fluid flow with surface roughness has attracted considerable attention, thus reports on several numerical and experimental studies have been published. A literature review on friction and heat/mass transfer in microchannels was prepared by Obot [3]. According to the available literature on microchannels, the arbitrary definition of microchannels is given with a hydraulic diameter of $D_h \leq 1,000 \mu\text{m}$ (1 mm). The main records are: (1) onset of transition to turbulent flow in smooth microchannels does not occur if the Reynolds number is less than 1,000, (2)

Nusselt number Nu varies as the square root of the Reynolds number in laminar flow. Effects of surface roughness on pressure drop and heat transfer in circular tubes was studied by Kandlikar et al. [4]. They reported, for single-phase flow in channels with small hydraulic diameters, that transition to turbulent flows occurs at Reynolds number values much below 2,300. Wen et al. [5] experimentally investigated the characteristics of the augmentation of heat transfer and pressure drop by different strip-type inserts in small tubes; they examined the effects of the imposed wall heat flux, mass flux and strip inserts on heat transfer rates. Surface roughness provoked surface friction was investigated by Guo and Li [6], who reported that frictional activity is responsible for the early transition from laminar to turbulent flow. The significance of viscous dissipation on the temperature field and on the friction factor was pointed out in the numerical and experimental investigations of [7]. Morini [8] worked on the role of the cross-sectional geometry on viscous dissipation and the minimum Reynolds number for which viscous dissipation effects cannot be neglected. The following works of [9, 10] described the roles of surface roughness on viscous dissipation, the resulting earlier transitional activity, increased friction factor values and head loss data. Wu and Cheng [11] reported that the laminar Nu and apparent friction coefficient increase with the increase of surface roughness, moreover the increase rates were determined to become more obvious at larger Reynolds numbers. Phares et al. [12] experimentally considered the pressure drop for liquid flow through short microtubes. Experimental investigations of [13], on dimpled tubes for laminar and transition flows, pointed out that the roughness induced friction factors were 10% higher than the smooth tube ones and the transition onset was at a relatively low Reynolds number of 1,400. Wall roughness effects in microtube flows were also considered by Engin et al. [14], who determined significant departures from the conventional laminar flow theory.

Due to its direct contribution to system performance, reliability and efficiency for long term applications, second-law analysis and entropy generation based investigations, on internal fluid flow related problems, have become more frequent recently. Lin and Lee [2] defined the effects of the fin tube spacing along spanwise direction on the second-law performance of wavy plate fin-and-tube heat exchangers. Sahin [15] analytically investigated entropy generation for a fully developed laminar viscous flow in a duct subjected to constant wall temperature and determined that for low heat transfer conditions the entropy generation due to viscous friction becomes dominant and the dependence of viscosity on temperature becomes essentially important in accurately determining the entropy generation. Passive heat transfer augmentation techniques, to conserve the useful part of energy (exergy) of single-phase flows, were reviewed by

Zimparov [16]. Ko [17] numerically investigated laminar forced convection and entropy generation in a helical coil with constant wall heat flux and suggested that the optimal Reynolds number is to be chosen according to the flow operating condition so that the thermal system can have the least irreversibility and best exergy utilization. Ko [18] also numerically performed the thermal design of plate heat exchanger double-sine ducts, from the point of entropy generation and exergy utilization. Ratts and Raut [19] obtained optimal Reynolds numbers for single-phase, convective, fully developed internal laminar and turbulent flows with uniform heat flux, by employing the entropy generation minimization method. Richardson et al. [20] investigated the existence of an optimum laminar flow regime, in singly connected microchannels with finite temperature differences and fluid friction, based on second-law analysis. Zimparov [21] investigated the effects of streamwise variation of fluid temperature and rib height to diameter ratio on the entropy production of a tubular heat exchanger with enhanced heat transfer surfaces. Rakshit and Balaji [22] reported the results of a numerical investigation of conjugate convection from a finned channel, where the vertical rectangular fins were mounted outside of the horizontal channel.

Roughness definition and impacts of roughness on the flow and heat transfer performances of various applications have been the main concern of some recent work, due to the fact that surface roughness constitutes a major role in systems with heat transfer and fluid flow. A few of the latest studies can be outlined as: the numerical works of Ozalp [23, 24] on compressible flow in converging and aerospace propulsion nozzles with various surface roughness conditions, Sahin et al.'s [25] study on entropy generation due to fouling as compared to that for clean surface tubes, non-equilibrium molecular dynamics simulation of Cao et al. [26] to investigate the effect of the surface roughness on slip flow of gaseous argon, Wang et al.'s [27] regular perturbation method to investigate the influence of two-dimensional roughness on laminar flow in microchannels between two parallel plates and Sheikh et al.'s [28] model to eliminate the discrepancy in the fouling measurements by characterizing the fouling as a correlated random process.

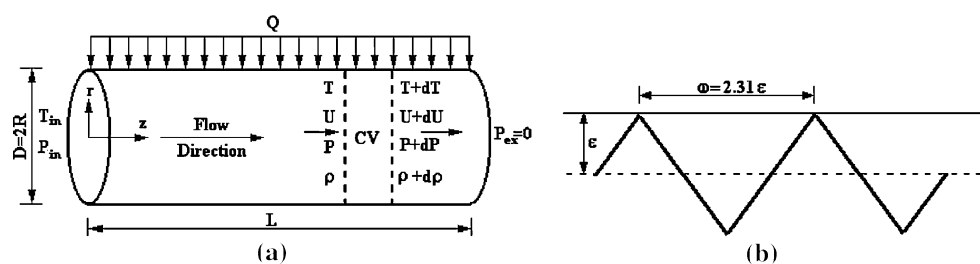
In spite of the fact that, the impacts of surface roughness on internal flow were widely investigated, the available literature, on circular duct flows with surface roughness and heat flux conditions, handles the fluid motion, heat transfer and second-law analysis separately. The present numerical work aims to develop a complete overview on the energy and exergy analysis of roughness induced forced convective laminar-transitional micropipe flow, for wide ranges of Reynolds number, surface roughness and heat flux. Momentum and energy transfer records are discussed through radial velocity and TP, boundary layer parameters, friction and discharge coefficients (C_d), Nu , frictional energy loss and mean-temperature variations in the flow direction, which also identifies the viscous dissipation rates. Exergy analysis results are presented by radial entropy profiles, thermal, frictional and overall entropy generation rates, irreversibility distribution and entropy generation aspect ratio values.

2 Theoretical background

2.1 Micropipe and roughness

The diameter and length of the micropipe (Fig. 1a), analyzed in the present paper, are given as D and L . The present roughness model is based on the triangular structure of Cao et al. [26] (Fig. 1b), where the roughness amplitude and period are characterized by ε and ω , respectively. The role of roughness on the heat and energy transfer performance of laminar-transitional flow is investigated by varying the amplitude in the range of $\varepsilon = 1\text{--}50\ \mu\text{m}$. However, in all computations the roughness periodicity parameter ($\omega' = \omega/\varepsilon$) is kept fixed to $\omega' = 2.31$, which corresponds to equilateral triangle structure (Cao et al. [26]). Equation 1 numerically characterizes the model of Cao et al. [26] with the implementation of the amplitude and period. The model function ($f_\varepsilon(z)$) is repeated in the streamwise direction throughout the pipe length, where the Kronecker unit tensor (δ_i) attains the values of $\delta_i = +1$ and -1 for $0 \leq z \leq \frac{2.31}{2}\varepsilon$ and $\frac{2.31}{2}\varepsilon \leq z \leq 2.31\varepsilon$, respectively.

Fig. 1 a Schematic view of circular pipe, b triangular surface roughness distribution



per unit volume (S'''), for a two-dimensional (r, z) compressible Newtonian fluid flow in cylindrical coordinates.

$$S''' = \frac{\kappa_f^T}{T^2} \left[\left(\frac{\partial T}{\partial r} \right)^2 + \left(\frac{\partial T}{\partial z} \right)^2 \right] + \frac{\mu^T}{T} \left[\left(\frac{\partial U}{\partial r} \right)^2 + 2 \left(\frac{\partial U}{\partial z} \right)^2 \right] \quad (11)$$

As given in Eq. 12a, the entropy generation due to finite temperature differences ($S'''_{\Delta T}$) in axial z and in radial r directions is defined by the first term on the right side of Eq. (11), the second term stands for the frictional entropy generation ($S'''_{\Delta P}$). Total and volumetric average entropy generation rates can be obtained by Eqs. 12b, c, and Eq. 12d stands for the irreversibility distribution ratio.

$$S''' = S'''_{\Delta T} + S'''_{\Delta P} \quad (12a)$$

$$S = 2\pi \int_{z=0}^{z=L} \int_{r=0}^{r=R} S''' r dr dz \quad (12b)$$

$$\bar{S}''' = \frac{S}{\pi R^2 L} \quad (12c)$$

$$\phi = \frac{S'''_{\Delta P}}{S'''_{\Delta T}} \quad (12d)$$

2.3 Computational method

The flow domain of Fig. 1a is divided into m axial and n radial cells ($m \times n$), where the fineness of the computational grids is examined to ensure that the obtained solutions are independent of the grid employed. Initial runs indicated an optimum axial cell number of $m = 500$, having an equal width of Δz , whereas the radial direction is divided into $n = 100$ cells. Since the velocity and temperature gradients are significant on the pipe walls, the 20% of the radial region, neighboring solid wall, is employed an adaptive meshing with radial-mesh width aspect ratio of 1.1. Forward difference discretization is applied in the axial and radial directions, for the two-dimensional marching procedure. The laminar micropipe flow with surface roughness and heat flux governs the complete equation set described above, which are highly dependent non-linear formulations, where the convergence problems and singularities are most likely to occur in the solution scheme of the sufficiently complex structure. For simultaneous handling, Eqs. (6–8) need to be assembled into the three-dimensional “Transfer Matrix”, consisting of the converted explicit forms of the principle equations. Direct simulation Monte Carlo (DSMC) method, as applied by Ozalp [23, 24] to compressible nozzle flow problems and by Wu and Tseng [30] to a micro-scale gas dynamics domain, is a utilized technique especially for internal gas

flow applications with instabilities. DSMC method can couple the influences of surface roughness and surface heat flux conditions over the meshing intervals of the flow domain. The benefits become apparent when either the initial guesses on inlet pressure and inlet velocity do not result in convergence within the implemented mesh, or if the converged solution does not point out the desired Reynolds number in the pipe. There exists two types of convergence problems (singularities) such that: (1) Mach number exceeds one inside the pipe and (2) the exit Mach number is lower than or equal to 1 but the exit pressure deviates from the related boundary condition more than 0.01 Pa (Eq. 3). Moreover, to enable the application of different types of boundary conditions with less specific change in programming, cell-by-cell transport tracing technique is adopted to support the Transfer Matrix scheme and to the DSMC algorithm. The concept of triple transport conservation is incorporated into the DSMC, which makes it possible to sensitively evaluate the balance of heat swept from the micropipe walls and the energy transferred in the flow direction and also to perform accurate simulation for inlet/exit pressure boundaries. To investigate the stream-wise variations of the three primary flow parameters (U, P, T), the resulting non-linear system of equations is solved by using the Newton–Raphson method. In the case of a convergence problem, U, P and T are investigated up to the singularity point, and then the local velocity is compared with that the inlet value together with the location of the singularity point w.r.t. to the inlet and exit planes. The inlet velocity is then modified by DSMC, by considering the type of singularity, the velocity variation and the corresponding pipe length. However inlet pressure and velocity are both modified, to increase or decrease the Reynolds number of the former iteration step, in the case that the Reynolds number does not fit the required value. Computations are based on the preconditions that, maximum allowable deviation of the exit pressure from the related boundary condition (Eq. 3) is less than 0.01 Pa and the convergence criteria for the mass flow rate throughout the flow volume is in the order of 0.01%. By simultaneously conserving mass flux and boundary pressure matching within the complete mesh, thermal equilibrium is satisfied at each pressure boundary in the flow volume.

3 Results and discussion

Numerical investigations are carried out in a micropipe having a diameter of $D = 1$ mm, which is consistent with the microchannel definition of [3]. As the pipe length is selected as $L = 0.5$ m, the inlet air temperature and exit pressure values are kept fixed to $T_{in} = 278$ K and $P_{ex} = 0$, respectively, throughout the work. To comprehensively

investigate the influences of Reynolds number, heat flux and surface roughness on the momentum-energy transport mechanisms and second-law of thermodynamics of roughness induced laminar-transitional flow, computations are performed for the ranges of $Re = 1\text{--}2,000$, $Q = 5\text{--}100\text{ W/m}^2$ and $\varepsilon = 1\text{--}50\text{ }\mu\text{m}$ ($\varepsilon^* = \varepsilon/D = 0.001\text{--}0.05$). The applied surface roughness values are similar to those of [27] ($\varepsilon^* = 0.005\text{--}0.05$), [14] ($\varepsilon^* \leq 0.08$) and [25] ($\varepsilon^* \leq 0.25$). Due to their contribution in entropy generation, discussions are based on radial velocity and TP, both for heating and viscous dissipation based cooling scenarios. Mean-temperature variations, momentum and heat transfer characteristics are handled by cross-correlations with radial, thermal, frictional and overall entropy generation mechanisms; by also considering the rates of power loss and entropy generation aspect ratio.

3.1 Momentum and energy transfer

3.1.1 Mean-temperature variations (ΔT)

Mean-temperature rise (ΔT) of the laminar-transitional flow in the Reynolds number range of $1 \leq Re \leq 2,000$ are presented for three heat flux and six non-dimensional surface roughness cases in Fig. 2a. It can be seen from the figure that, independent of the intensity of heat flux, there exists a reverse relation among the Re and ΔT values; in

fact this can also be expressed as the higher impressive character of heat flux at lower mass flow rates. Numerically it can more specifically be identified that for the $Q = 5\text{ W/m}^2$ case the partial derivative of $\frac{\partial \Delta T}{\partial Re}$ attains the values of -76.1 , -6.34 and -0.07 for Re of 1, 10 and 100, respectively. Besides, augmentation of the heat flux values are accompanied with higher temperature rise data in the complete Reynolds number range. However, computations point out that the role of heat flux on temperature rise is more remarkable at low Reynolds number cases, such as for the heat flux case of $Q = 5\text{ W/m}^2$ at $Re = 10, 100$ and 1,000 the partial derivative of $\frac{\partial \Delta T}{\partial Re}$ is evaluated as -6.34 , -0.07 and -0.004 ; whereas these values rise to -48.63 , -1.25 and -0.016 for $Q = 100\text{ W/m}^2$. These proportions additionally indicate that the role of Reynolds number, thus mass flow rate, on temperature rise becomes more comprehensible at higher heat flux applications. Figure 2a further interprets the influence of surface roughness on ΔT values. At low Reynolds numbers, computations showed that the role of ε^* on ΔT is ignorable. But, in the cases with higher Re the deviations become recognizable where the application of higher surface roughness results in lower mean-temperature variations. Defining the identifiable deviation by 1% shift of the two limiting non-dimensional surface roughness cases, with the formula of $\left(\frac{\Delta T_{\varepsilon^*=0.05} - \Delta T_{\varepsilon^*=0.001}}{\Delta T_{\varepsilon^*=0.001}} \times 100\right) = 1$, points out the onset Reynolds numbers of $Re = 79, 425$ and 528 for the heat

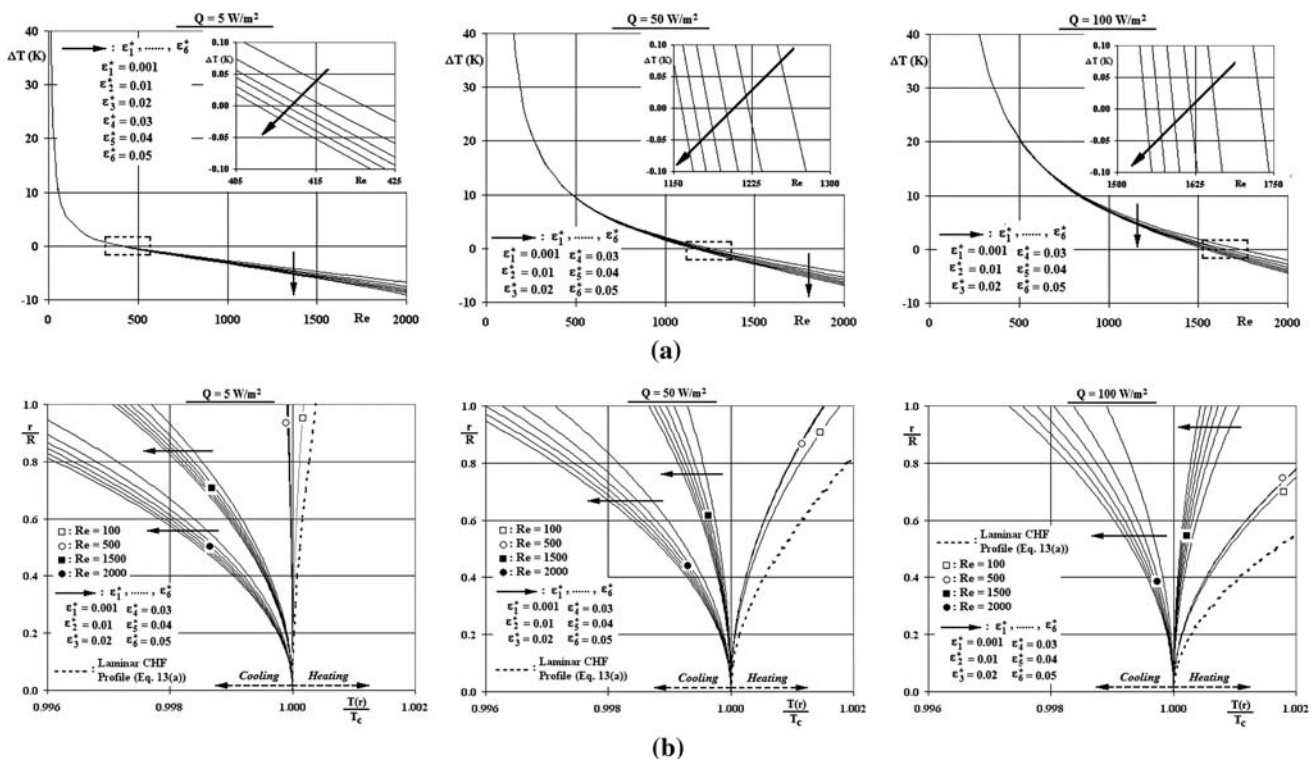


Fig. 2 Variations of **a** mean-temperature values, **b** radial temperature profiles with Re , ε^* and Q

flux values of $Q = 5, 50$ and 100 W/m^2 , respectively. These limits put forward that higher heat flux values narrows the influential Re range of ε^* on ΔT in laminar flow. On the other hand Fig. 2a shows that, although heat is added through the lateral walls of the circular pipe, beyond certain Reynolds numbers the flow temperature decreases in the axial direction. To provide a deeper insight for the cooling outputs, Table 1 shows the applied flux and the corresponding total surface heat transfer values (Q_s), together with the amount of viscous energy loss data (ψ_{loss}) for five Reynolds numbers and also for the surface roughness range of $\varepsilon^* = 0.001$ (ε_1^*)– 0.05 (ε_6^*). In the case with $Q = 5 \text{ W/m}^2$, the total heat added through the duct walls ($Q_s = 7.85 \times 10^{-3} \text{ W}$) is lower than the energy loss values for $Re = 500$ for the complete ε^* range ($\psi_{\text{loss}} = 1.11 \times 10^{-2}$ – $1.21 \times 10^{-2} \text{ W}$), where the gap between the Q_s and ψ_{loss} values rise in the cases with higher Re . The tabulated data is projected to Fig. 2a with augmented cooling behavior with the increase of Reynolds number. Particularly, the thermally critical Reynolds numbers ($(Re_{\text{cr}})_{\text{th}}$) can be visualized through the zoomed plots of Fig. 2a and determined as $(Re_{\text{cr}})_{\text{th}} \approx 414 \pm 7$, $\approx 1,210 \pm 50$ and $\approx 1,635 \pm 85$ for $Q = 5, 50$ and 100 W/m^2 , respectively, where the lower and upper limits refer to the non-dimensional surface roughness applications of $\varepsilon_6^* = 0.05$ and $\varepsilon_1^* = 0.001$. It can be seen that $(Re_{\text{cr}})_{\text{th}}$ increase with higher heat flux; moreover the enhanced impact of ε^* on ΔT values at higher Q are also clarified with the expanded $(Re_{\text{cr}})_{\text{th}}$ limits. Energy loss and temperature decrease due to friction in laminar flow was also reported in recent works by Koo and Kleinstreuer [7], Morini [8] and Celata et al. [9, 10]. Their common findings are wall heating due to viscous dissipation; the dissipated energy resulted in loss of flow temperature even the surface roughness effects were disregarded. Additionally they also indicated that, viscous dissipation is directly related with Reynolds number where they experimentally and numerically recorded exponential augmentations in energy loss due to high Re . These results show harmony with the present evaluations on heating/cooling behaviors of Fig. 2a and the energy loss data of Table 1.

3.1.2 Radial temperature profiles

The radial variations of temperature values, in non-dimensional form w.r.t. to the centerline value (T_c), for various heat flux, surface roughness and Reynolds numbers are displayed in Fig. 2b. Since the development of TP is based both on energy loss (ψ_{loss}) due to viscous dissipation on the solid walls and surface heat transfer rates, the computed profiles are presented in conjunction with the laminar constant heat flux formula of Eq. 13a, where α is the thermal diffusivity (Eq. 13b).

$$T(r) = T_s - \frac{2U_o R^2}{\alpha^T} \left(\frac{dT_o}{dz} \right) \left[\frac{3}{16} + \frac{1}{16} \left(\frac{r}{R} \right)^4 - \frac{1}{4} \left(\frac{r}{R} \right)^2 \right] \tag{13a}$$

$$\alpha^T = \frac{k_f^T}{\rho C_p^T} \tag{13b}$$

It can be seen from the figure that the TP of the flows for $Re \leq 500$ did not experienced the influence of surface roughness, resulting in coinciding TPs for the complete ε range investigated. This outcome is completely in harmony with the temperature rise discussions through Fig. 2a. On the other hand, with the increase of flow velocity, thus Reynolds number ($Re > 500$), the role of surface roughness becomes apparent. For the lowest heat flux case of $Q = 5 \text{ W/m}^2$, the TP of $Re = 100$ is very similar to the laminar constant heat flux profile (Eq. 13a). The slight deviation can be explained by the low power loss rates that are in the order of $\psi_{\text{loss}} = \sim 4.4 \times 10^{-4} \text{ W}$. However, for the same Reynolds number case of $Re = 100$, with the increase of heat flux values ($Q = 50$ and 100 W/m^2) the power loss values also rise (Table 1), due to the augmented flow viscosity with higher flow temperatures, which result in comparably more evident shifts in TPs from that of Eq. 13a. The increase in Reynolds numbers brings about significant variations in the TPs, which can be attributed to the elevated power loss amounts as given in Table 1. Heating of the flowing air is computed for the condition of $\psi_{\text{loss}} < Q_s$, but in the cases where viscous dissipation dominates the surface heat addition ($\psi_{\text{loss}} > Q_s$) cooling is

Table 1 ψ_{loss} values for various Re , ε^* and Q cases

Q (W/m^2)	5	50	100
Q_s (W)	7.85×10^{-3}	7.85×10^{-2}	1.57×10^{-1}
ψ_{loss} (W) (ε_1^* – ε_6^*)			
$Re = 100$	4.38×10^{-3} – 4.46×10^{-4}	5.63×10^{-4} – 5.72×10^{-4}	7.34×10^{-4} – 7.44×10^{-4}
$Re = 500$	1.11×10^{-2} – 1.21×10^{-2}	1.17×10^{-2} – 1.27×10^{-2}	1.24×10^{-2} – 1.34×10^{-2}
$Re = 1,000$	4.68×10^{-2} – 5.49×10^{-2}	4.80×10^{-2} – 5.63×10^{-2}	4.94×10^{-2} – 5.78×10^{-2}
$Re = 1,500$	1.11×10^{-1} – 1.41×10^{-1}	1.13×10^{-1} – 1.43×10^{-1}	1.15×10^{-1} – 1.45×10^{-1}
$Re = 2,000$	2.08×10^{-1} – 2.85×10^{-1}	2.10×10^{-1} – 2.89×10^{-1}	2.13×10^{-1} – 2.92×10^{-1}

the outcome, where the thermally critical Reynolds numbers are as described in Fig. 2a. Figure 2b also shows that, the role of surface roughness grows with Reynolds number, especially in the flows with decreasing mean flow temperatures. Table 1 indicates the power loss amounts for the low flux case of $Q = 5 \text{ W/m}^2$ as $\psi_{\text{loss}} = 1.11 \times 10^{-1} - 1.41 \times 10^{-1} \text{ W}$ ($\varepsilon_1^* - \varepsilon_6^*$) and $\psi_{\text{loss}} = 2.08 \times 10^{-1} - 2.85 \times 10^{-1} \text{ W}$ for $Re = 1,500$ and $2,000$, respectively; these ranges rise to $\psi_{\text{loss}} = 1.15 \times 10^{-1} - 1.45 \times 10^{-1}$ and $\psi_{\text{loss}} = 2.13 \times 10^{-1} - 2.92 \times 10^{-1}$ for the highest heat flux of $Q = 100 \text{ W/m}^2$. The rise of the ψ_{loss} values with heat flux can be attributed to the augmented viscosity values at higher temperature values, being an outcome of the elevated streamwise temperature values. The deviations of the TPs from the CHF profile for the complete set of applied surface heat fluxes, become more recognizable at higher Reynolds numbers and surface roughness conditions, which clearly puts forward that the viscous dissipation and the associated frictional energy loss rates augment with both Re and ε . Ozalp [23, 24] also determined augmented frictional power loss records in compressible high speed converging nozzle with increase of surface heat flux. The tabulated power loss values also indicate that the gap among the lower and upper ψ_{loss} limits enlarge significantly with Reynolds number and secondarily with surface heat flux. The common determination from Fig. 2a, b and Table 1 can be summarized as the necessity of considering the amount of viscous dissipation in the flow domain before deciding the heat flux level to match the required heating/cooling activity in a micropipe.

3.1.3 Radial velocity profiles

Variations in the velocity profiles (VP), in the presence of surface roughness and heat flux conditions are displayed in Fig. 3. Computational results are shown in conjunction with the characteristic profiles for the laminar and turbulent

flows. The laminar profile and the modified turbulent logarithm law for roughness are given by Eqs. 14a, b (White [31]), respectively, where U^* is the friction velocity (Eq. 14c). Additionally, the boundary layer parameters like shape factor (Eq. 15a), friction coefficient (Eq. 16a), and also in normalized form (Eq. 16c) are evaluated. Moreover to describe the flow regime, the computed shape factor values are compared with the characteristic laminar ($H_{\text{lam}} = 3.36$) and turbulent ($H_{\text{turb}} = 1.70$) data, resulting in the intermittency (γ) values (Eq. 15b), where the defined boundary parameters are given in tabulated form for various Reynolds numbers within the plots. Computations indicated no change in the VPs with the application of different heat flux values, thus the presented VP curves designate the combined influences of Re and ε^* on the VP formation. At the upper Reynolds number limit of $Re = 2,000$, computations pointed a maximum Mach number of $M = 0.083$, which results in a streamwise density variation of 2.42%. Thus the VP, given in Fig. 3, represent the flow characteristics for the complete pipe length.

$$\frac{U(r)}{U_o} = 2 \left[1 - \left(\frac{r}{R} \right)^2 \right] \tag{14a}$$

$$\frac{U(r)}{U^*} = 2.44 \ln \left(\frac{R-r}{\varepsilon} \right) + 8.5 \tag{14b}$$

$$U^* = \sqrt{\frac{\tau_w}{\rho}} \tag{14c}$$

$$H = \frac{\int_{r=0}^{r=R} \left(1 - \frac{U(r)}{U_m} \right) r dr}{\int_{r=0}^{r=R} \frac{U(r)}{U_m} \left(1 - \frac{U(r)}{U_m} \right) r dr} \tag{15a}$$

$$\gamma = \frac{H_{\text{lam}} - H}{H_{\text{lam}} - H_{\text{turb}}} \tag{15b}$$

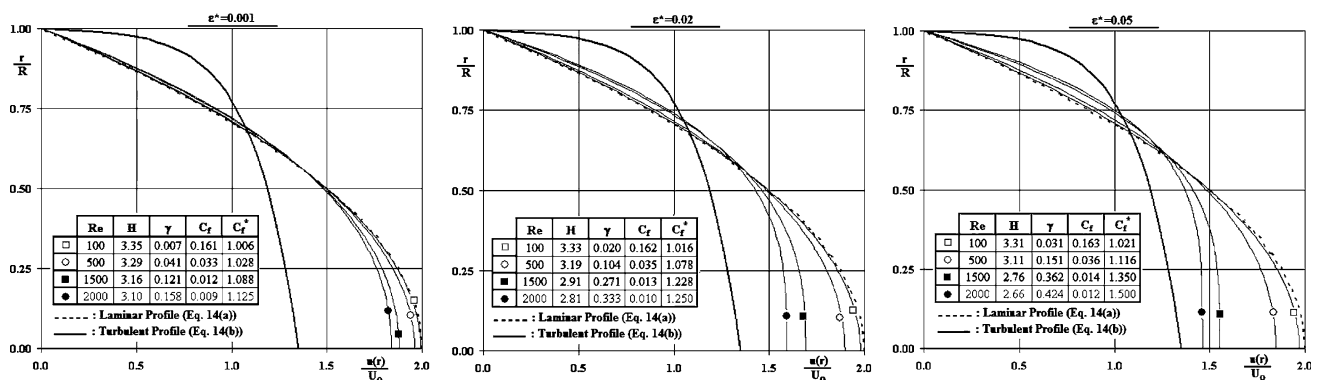


Fig. 3 Variations of radial velocity profiles with Re and ε^*

$$C_f = \frac{2\mu^T \left| \frac{dU}{dr} \right|_{r=R}}{\rho_o U_o^2} \quad (16a)$$

$$(C_f)_{\text{lam}} = \frac{16}{Re} \quad (16b)$$

$$C_f^* = \frac{C_f}{(C_f)_{\text{lam}}} \quad (16c)$$

Figure 3 shows that the VP of the case with $Re = 100$ was not affected by surface roughness, where the highest ε^* of 0.05 was not influential enough to create a shift in the VP from that of the laminar. For the surface roughness range of $\varepsilon^* = 0.001$ –0.05, the H and γ are evaluated as $H = 3.35$ –3.31 and $\gamma = 0.007$ –0.031, denoting the laminar character. As the Reynolds number is increased, the impact of surface roughness on the VP becomes more apparent. Such as, at $Re = 500$ the highest surface roughness in the computations ($\varepsilon^* = 0.05$) caused significant and clear shifts in the VP from that of the laminar with a lower shape factor ($H = 3.11$), a higher intermittency ($\gamma = 0.151$) and a higher normalized friction coefficient ($C_f^* = 1.116$). Transition onset in internal flow problems with surface roughness was considered in the related experimental and numerical investigations. Although a common decision does not exist, several researchers [3, 4, 6, 13, 32] recognize a 10% rise in C_f , which corresponds to $C_f^* = 1.1$, above the traditional laminar formula of Eq. 16b as an indicator for the transitional activity. As can be seen from Fig. 3, in the present work normalized friction coefficients of $C_f^* = 1.1$ are evaluated at the Reynolds numbers of $Re_{\text{tra}} = \sim 1,650$, ~ 575 and ~ 450 for ε^* of 0.001, 0.02 and 0.05, respectively, where the corresponding intermittency values are $\gamma = 0.132$, 0.117 and 0.136. The determined Re_{tra} are in harmony with the records of [3] ($Re_{\text{tra}} \approx 2040$ for inconsiderable roughness), Kandlikar et al. [4] ($Re_{\text{tra}} \approx 1,700$ for $\varepsilon^* \approx 0.003$) and Wu and Little [32] ($Re_{\text{tra}} \approx 510$ –1,170 for a wide range of ε^*). Distinguishing $C_f^* = 1.1$ as an indicator for transition not only indicates that roughness accelerates transition to lower Reynolds numbers but also puts forward that transition onset can also be determined through intermittency data, where the present computations perceive the γ range of ~ 0.1 –0.15 for transition onset. On the other hand, the C_f^* values showed also augmentation with Re , such that as C_f^* is evaluated as 1.006, 1.028 and 1.088 for $Re = 100$, 500 and 1,500, respectively, at $\varepsilon^* = 0.001$, the corresponding values rise to $C_f^* = 1.021$, 1.116 and 1.350 at $\varepsilon^* = 0.05$. Guo and Li [6], Wang et al. [27] and Engin et al. [14] also reported the augmented role of roughness on friction coefficient with Reynolds number. The wall velocity gradient $\left(\frac{dU}{dr} \right)_{r=R}$ has direct contribution in the friction factor values. Moreover the VPs, especially the near wall

regions ($r/R \geq 0.75$) and the centerline ($r/R = 0$) put forward the growing influence of surface roughness on the flow pattern with Reynolds number. The gap between the U_c/U_o ratios and the traditional data of $U_c/U_o = 2.0$ (Eq. 14a) increases both with higher ε^* and Re , which can also be attributed to the grow of C_f and C_f^* in the investigated scenarios. Figure 3 clarifies the impact of surface roughness in laminar flow by putting forward the VP transformation from laminar to the initial stages of transitional character with ascends in C_f^* and γ and descends in H and U_c/U_o values with higher ε^* .

3.1.4 Discharge coefficients

The frictional forces, acting on the flow, have a resistive role, which results in lower mass flow rates when compared to that of isentropic flows. Since C_d is defined as the ratio of the real and isentropic flow rates (Eq. 17a), it is an indicator not only for the amount of the frictional character and also for the loss of streamwise momentum due to lower mass flow rates. Variation of C_d values with Reynolds number for various ε^* cases is displayed in Fig. 4a for the heat flux case of $Q = 5 \text{ W/m}^2$; the present numerical values are also compared with the analytical solutions of [12] (Eq. 17b) and [33] (Eq. 17c). Table 2 additionally displays the impact of surface heat flux on C_d together with the considered Re and ε^* ranges. The plotted and tabulated data indicate not only that the C_d values increase with Re and decrease with ε^* , but also the C_d ranges expand in higher Reynolds number cases revealing the enhanced role of ε^* on the flow rate values. This outcome is harmony with the discussions on C_f^* – Re interactions of Fig. 3 where C_f^* values were expressed to rise with ε^* but to decrease with Re . Ozalp [23, 24] reported similar findings on the C_d – ε^* relation in compressible converging nozzle flows.

$$C_d = \frac{\dot{m}_{\text{real}}}{\dot{m}_{\text{isen}}} \quad (17a)$$

$$C_d = \frac{1}{8} \left(\frac{D}{L} \right)^{0.5} Re^{0.5} \quad (17b)$$

$$C_d = \frac{\dot{m}}{\rho A} \left(\frac{\rho}{2\Delta P} \right)^{0.5} \quad (17c)$$

Additionally, Table 2 interprets the slight decrease of C_d data with heat flux values, which is a consequence of higher viscosity, frictional forces and power loss values as discussed through Table 1. It can be seen from Fig. 4a that, the computational C_d values for the highest roughness scenario of $\varepsilon^* = 0.05$ are consistent with the equation of [12] for the complete Reynolds number range. On the other hand, although quite close, the proposed equation of [12] deviate from that of [33] for $Re > 500$. However, either of

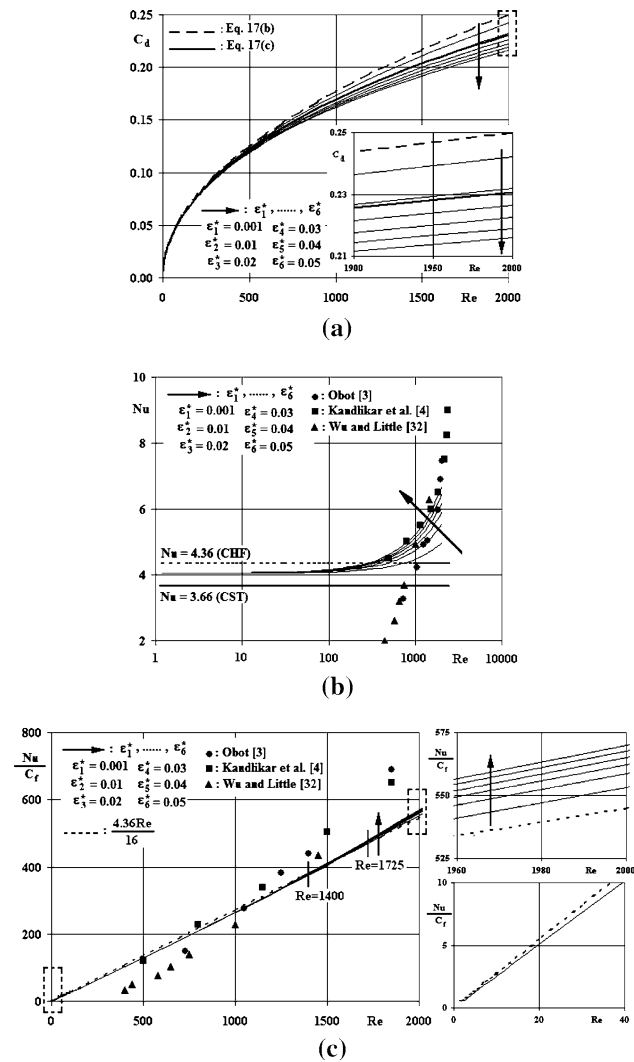


Fig. 4 Variations of **a** C_d , **b** Nu , **c** Nu/C_f values with Re and ε^*

the methods show significant similarities with the present evaluations for $Re < 1,000$. The zoomed plot for the Reynolds number range of 1,900–2,000 put forward the inconsistency of Eqs. 17b, c with the high ε^* cases at high Re . This outcome can be explained by the facts that: in the present work the flow turns out to be of transitional type at

low Reynolds numbers due to surface roughness; moreover neither of the analytical solutions involve surface roughness as an effective parameter on the momentum rates.

3.1.5 Nusselt numbers

Variation of Nu , in the presence of surface roughness and for the Reynolds number range of 1–2,000 are displayed in Fig. 4b. Computations indicated that surface roughness and flow velocity were not influential on heat transfer rates below $Re = 100$, where Nu was within the limits of $Nu = 4.36$ and $Nu = 3.66$, which are the traditional laminar values for constant heat flux and constant surface temperature cases, respectively. In spite of the almost-fixed Nu of 4.04 for $Re < 100$, with the increase of Re heat transfer rates are also evaluated to rise. Similar to the present records, the heat transfer measurements Vicente et al. [13] pointed out constant Nu of ~ 4.36 for $Re < 700$, then after increase of Nu was recorded. The present computations additionally put forward that surface roughness plays an increasing role on Nu , where the impact becomes apparent for $Re > 100$. Experiments of [4], for the ε^* range of 0.0018–0.0028, also pointed augmentations in Nu with surface roughness. Besides, although the heat transfer reports of [32] were lower than the present evaluations for $Re < 1,000$, the experimental data of [3] (for $Re \geq 1,000$), [32] (for $Re \geq 1,000$) and [4] (for $Re \geq 500$) are reasonably in harmony with the current numerical outputs. On the other hand, the present computations resulted in the $Nu_{\varepsilon^*=0.05}/Nu_{\varepsilon^*=0.001}$ ratios of 1.086, 1.168 and 1.259 for $Re = 500, 1,000$ and $1,500$, which clearly denote that the influence of ε^* on Nu grows with Re , which is in harmony with the experimental reports of [11]. Augmentations in heat transfer rates with Reynolds number are also significant from the point of transition, where the recent related studies [3, 4, 13, 32] consider 15–20% rise in Nu with Re as an indicator for transition. Adopting the Re_{tra} values, determined in Sect. 3.1.3, to the heat transfer investigations result in the $Nu_{Re_{tra}}/Nu_{Re=1}$ ratios of 1.18, 1.12 and 1.11 for Re_{tra} of 1,650 ($\varepsilon^* = 0.001$), 575 ($\varepsilon^* = 0.02$) and 450

Table 2 C_d values for various Re , ε^* and Q cases

Q (W/m ²)	C_d				
	Computational ($\varepsilon_1^*-\varepsilon_6^*$)				
	5	50	100	Equation 17b	Equation 17c
$Re = 100$	0.0553–0.0549	0.0511–0.0507	0.0471–0.0468	0.0559	0.0551
$Re = 500$	0.1237–0.1190	0.1216–0.1171	0.1195–0.1152	0.1250	0.1223
$Re = 1,000$	0.1735–0.1618	0.1722–0.1607	0.1707–0.1594	0.1768	0.1696
$Re = 1,500$	0.2110–0.1919	0.2100–0.1911	0.2089–0.1902	0.2165	0.2037
$Re = 2,000$	0.2423–0.2160	0.2414–0.2154	0.2405–0.2147	0.2500	0.2307

($\varepsilon^* = 0.05$), respectively. These ratios show similarity with those of [3, 4, 13, 32]; moreover they also indicate that the present computational analysis on flow and heat transfer characteristics coincide from the point of transition onset.

3.1.6 Cross-correlations with friction factor (Nu/C_f)

As described above, surface roughness augments both heat transfer rates and friction factor values; thus the question of “Whether Nu or C_f is more considerably influenced by surface roughness?” arises. Figure 4c displays the variation of the computational Nu/C_f ratios with Re , where the present results are not only compared with those of the recent work but also with the traditional ratio of $4.36Re/16$ for laminar flow with constant heat flux. It can be seen from the figure that, up to $Re \approx 1,400$ ($\varepsilon^* = 0.05$)– $1,725$ ($\varepsilon^* = 0.001$) the affect of ε^* on C_f is higher than its impact on Nu , which in return result in lower Nu/C_f ratios than the traditional line. Moreover, the zoomed plot for $0 < Re < 40$ puts forward that the level of roughness amplitude is not affective on the ratio, where this range extends up to $Re \approx 500$. Beyond the Re limit of $1,400$ – $1,725$, the role of ε^* on heat transfer and friction factor characteristics inversely change, resulting in the rise of Nu/C_f ratios above the traditional line. Additionally, in the same Reynolds number range the influential character of roughness amplitude level becomes apparent. The zoomed plot for $1,960 < Re < 2,000$ clearly puts forward that at high Re , surface roughness augments heat transfer rates more remarkably than friction factors and this determination becomes important at high ε^* cases. The works of [4] concluded in similar outputs with the present study. At low Re their Nu/C_f ratios were either lower than or compatible with the traditional line; however with the increase of Reynolds number their findings as well elevated above the traditional line.

3.2 Exergy analysis

3.2.1 Entropy generation

3.2.1.1 Radial entropy profiles Combined influences of Reynolds number, surface roughness and surface heat flux on the radial entropy profiles are demonstrated in Fig. 5. It can be seen from the figure that, being independent of Reynolds number, entropy generation at the pipe centerline is comparably lower than those at the wall. It is determined that, at low Reynolds numbers of $Re \leq 500$ (Fig. 5a, b) centerline entropy values augment significantly with the increase of heat flux. As can also be inspected from Fig. 2b that, application of higher Q resulted in elevated temperature gradients ($\partial T/\partial y$) at the centerline. Since the discussions on VP (Fig. 3) emphasized the fact that VPs were not influenced by heat flux, the rise of entropy values

can be explained by the rise of centerline temperature gradients. On the other hand, minor entropy augmentations are recorded at the pipe wall with Q , which are rather secondary when compared with those of the centerline. The reason can be rationalized by the negligible rise of wall temperature gradient values with heat flux (Fig. 2b); the resulting slight entropy augmentations at the pipe wall can be visualized at the zoomed plots for the radial region of $0.7 \leq r/R \leq 1.0$ for $Re = 100$ and 500 (Fig. 5a, b). As was also implied in Figs. 2, 3, at low Reynolds number cases surface roughness had no contribution on the VPs and TPs. As a consequence, the entropy profiles for different ε^* cases at $Re = 100$ are overlapping (Fig. 5a). On the other hand, the zoomed plots for $0.00 \leq r/R \leq 0.02$ and $0.7 \leq r/R \leq 1.0$ put forward that in the centerline neighborhood, ε^* decreases entropy values whereas the contrary impact is evaluated at near wall regions. This outcome can be explained by the augmented intermittency values of Fig. 3 for $Re = 100$ with ε^* . Figure 3 puts forward that higher ε^* values result in, although comparably slight, fuller VP, having smoother appearances (low gradients) at the centerline and sharper character (high gradients) on the wall. The VP formation with ε^* is the source of impact-reversal of ε^* on S' , where the radial location can be indicated by $r/R = 0.80$ for $Re = 100$, as demonstrated in the zoomed of Fig. 5a. On the other hand, with the increase of Reynolds number, the role of surface roughness on entropy generation becomes more evident. Comparing Fig. 5a–c propose that not only the deviation of ε^* based entropy profiles grows with Re but also the entropy values significantly augment with Re . Although the entropy values at $r/R = 0$ are comparable in the complete Re range considered, in the radial direction toward the pipe wall the augmentations in S' values become apparent, where the maximum increase locations are determined as the pipe walls. Computations also indicate that the radial location of impact-reversal of ε^* on S' is independent of the applied heat flux and shifts toward pipe wall with Re ; such that for $Re = 500$ and $1,500$ the locations are determined as $r/R = 0.81$ and 0.825 , respectively. As can be seen from Fig. 5 that, entropy values are evaluated to decrease in the pipe wall neighborhood ($r/R \geq 0.99$) for all heat flux values and Reynolds numbers; the similar outcome was also reported by Ko [17] for $r/R \geq 0.90$. Combined influences of Re , ε^* and Q on the total volumetric entropy generation values (\bar{S}''') are also shown in Table 3. The rise of the entropy values with Reynolds number is displayed in Table 3, where Rakshit and Balaji [22], for a finned channel flow, and Zimparov [21], for a constant wall temperature duct flow, reported similar findings. The tabulated data for the low velocity case of $Re = 100$ are in harmony with Fig. 5a, putting forward the negligible role of ε^* on \bar{S}''' values for the complete Q range. However at

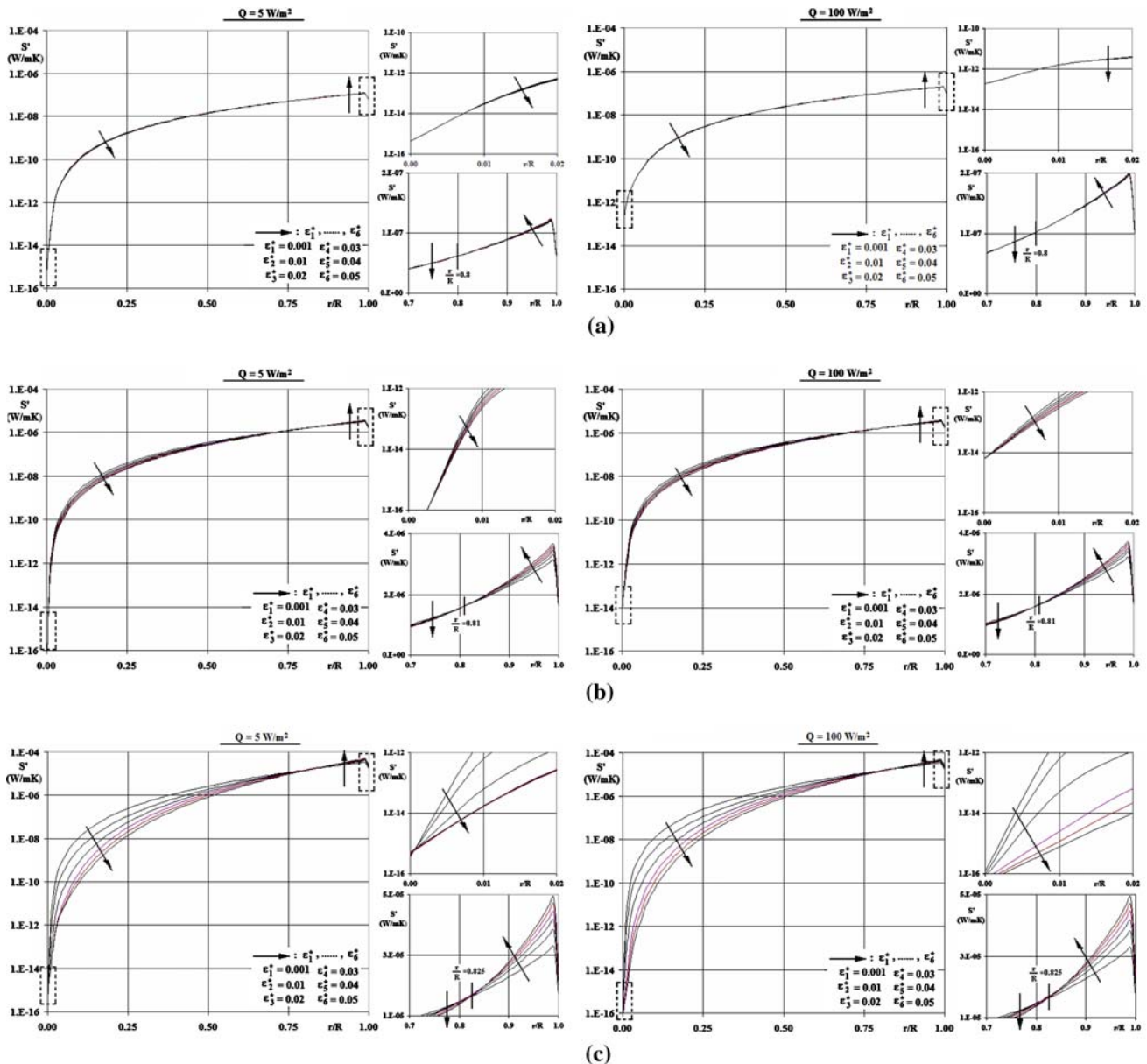


Fig. 5 Variations of radial entropy profiles with ε^* and Q at **a** $Re = 100$, **b** $Re = 500$, **c** $Re = 1,500$

higher Reynolds number flows the role of roughness becomes visible where the $\bar{S}'''_{\varepsilon^*=0.05} / \bar{S}'''_{\varepsilon^*=0.001}$ ratio attains the flux independent values of 1.03 and 1.09 at $Re = 1,000$ and $2,000$, respectively. The augmentation in the ratio is not only an indicator of the more influential character of ε^* at high Re but also put forward that entropy generation due to surface roughness becomes more remarkable with the rise of intermittency data (Fig. 3) and due to the transitional character. Table 3 additionally interprets the significant increase rates in the \bar{S}''' values at $Re = 100$ with higher heat flux applications. As the ratio of $\bar{S}'''_{Q=50} / \bar{S}'''_{Q=5}$ is 1.30 for $Re = 100$, it decreases to ~ 1.006 for $Re = 2,000$. The minor ratio at $Re = 2,000$ is due to the slightly higher

temperature values ($\sim 2^\circ\text{C}$ —Fig. 2a) at $Q = 50 \text{ W/m}^2$, that causes minor grows in flow viscosity and frictional activity.

3.2.1.2 Radial irreversibility distribution (ϕ) profiles Since the generated entropy is composed of two terms, $\bar{S}'''_{\Delta T}$: the thermal part and $\bar{S}'''_{\Delta P}$: the frictional part, a deeper survey by decomposing the overall generation rate into sub-sections will be helpful in understanding the entropy mechanism. Irreversibility distribution (ϕ), as defined by Eq. 12d, is the ratio of the frictional ($\bar{S}'''_{\Delta P}$) to thermal ($\bar{S}'''_{\Delta T}$) based entropy generations. It can be seen from Fig. 6a that, being independent of Re , ε and Q , in the

Table 3 \bar{S}''' values for various Re , ε^* and Q cases

Q (W/m ²)	\bar{S}''' (W/m ³ K)								
	5			50			100		
Re	100	1,000	2,000	100	1,000	2,000	100	1,000	2,000
$\varepsilon^* = 0.001$	3.89	400.75	1,709.43	5.05	407.20	1,720.42	6.95	415.56	1,734.11
$\varepsilon^* = 0.01$	3.89	403.90	1,773.08	5.05	410.32	1,784.41	6.95	418.67	1,798.23
$\varepsilon^* = 0.02$	3.89	406.71	1,784.82	5.05	413.14	1,795.95	6.95	421.48	1,809.62
$\varepsilon^* = 0.03$	3.89	409.49	1,805.38	5.05	415.92	1,816.22	6.95	424.26	1,829.66
$\varepsilon^* = 0.04$	3.89	412.33	1,834.13	5.05	418.74	1,844.78	6.95	427.11	1,857.99
$\varepsilon^* = 0.05$	3.89	415.28	1,868.88	5.05	421.74	1,879.45	6.95	430.07	1,892.48

entire flow scenarios irreversibility distribution vanishes at the centerline ($r/R = 0$) of the pipe. This not only indicates that the major portion of the total entropy generation is thermal based ($\bar{S}_{\Delta T}'''$) but also validates that the frictional activity ($\bar{S}_{\Delta P}'''$) in the centerline region is negligible. Whereas, due to the fact that considerable frictional activity and also the elevated velocity gradients are evaluated near the solid boundary (Fig. 3), ϕ attains the highest values at the solid wall ($r/R = 1$). Figure 6a additionally indicates that in the cooling scenarios of $Q = 5$ W/m² and $Re \gtrsim 414$, $Q = 50$ W/m² and $Re \gtrsim 1,210$,

$Q = 100$ W/m² and $Re \gtrsim 1,635$ (Fig. 2a) irreversibility distribution data, in the entire radial domain ($0 < r/R < 1$), decreases with higher surface roughness (Fig. 6a). But in heating, high wall temperatures cause flow viscosity values to rise locally, which result in augmented frictional activity in the regions close to the pipe walls, causing the $\bar{S}_{\Delta P}'''$ portion to increase in the total generation. As a result, in heating scenarios it is evaluated that the impact of ε^* on ϕ at the centerline ($r/R = 0$) and solid wall ($r/R = 1$) neighborhoods is opposite. This structure becomes identifiable especially in the cases of $Re = 500$ –1,000 and

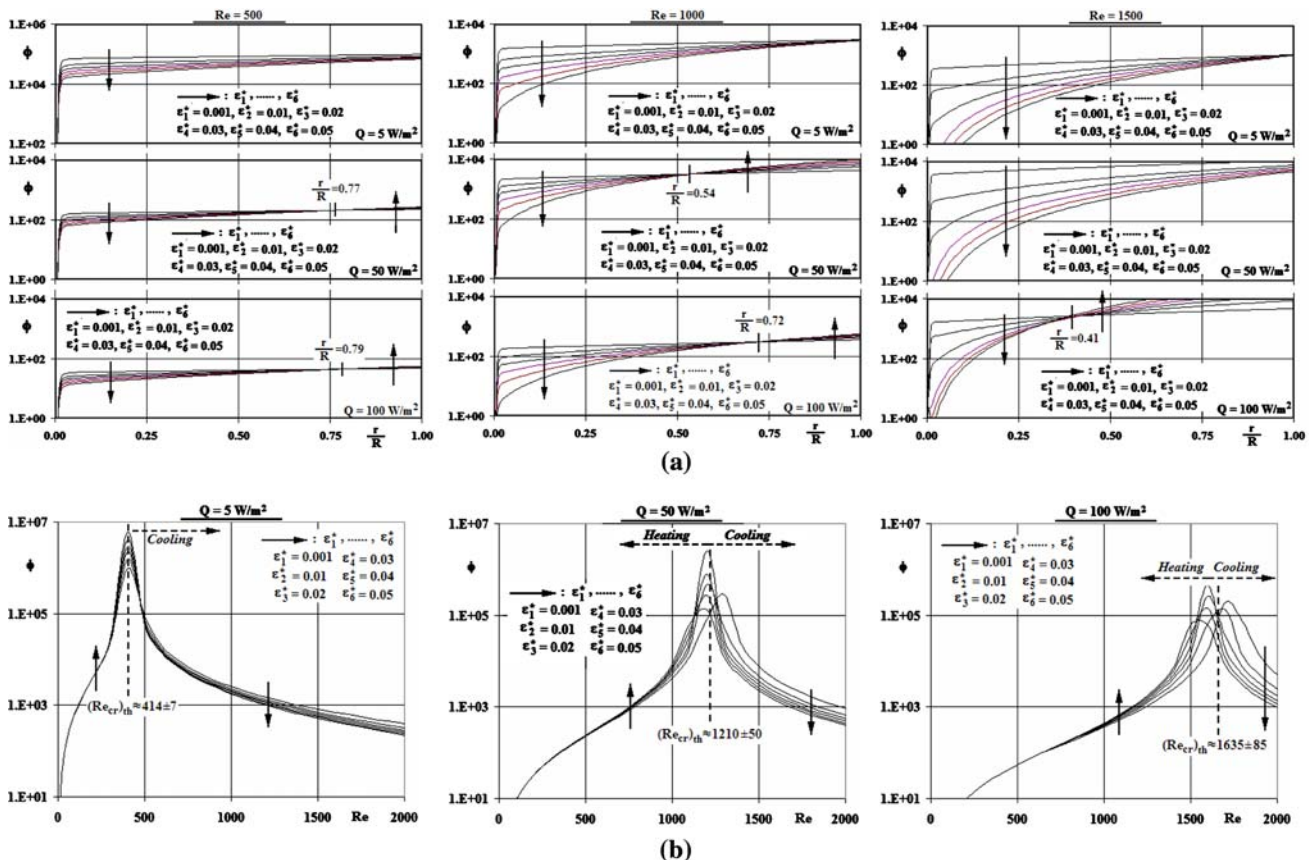


Fig. 6 Variations of **a** radial ϕ profiles, **b** ϕ numbers with Re , ε^* and Q

$Q = 50 \text{ W/m}^2$ and $Re = 1,000\text{--}1,500$ and $Q = 100 \text{ W/m}^2$. Besides, Fig. 6a points out that, the near-wall increasing role of ε^* on ϕ becomes stronger for fixed heat flux values with Reynolds number; additionally, the radial region of the heating-based increasing role, also enlarges. Such that for $Q = 50 \text{ W/m}^2$, as the defined region is $0.77 \leq r/R \leq 1$ for $Re = 500$, the corresponding one is $0.54 \leq r/R \leq 1$ for $Re = 1,000$; whereas at the heat flux of $Q = 100 \text{ W/m}^2$ for $Re = 500, 1,000$ and $1,500$ these radial zones become $0.79 \leq r/R \leq 1$, $0.72 \leq r/R \leq 1$ and $0.41 \leq r/R \leq 1$, respectively.

3.2.1.3 Irreversibility distribution (ϕ) variation In addition to the radial variations of irreversibility distribution, dependence of ϕ on Reynolds number needs deeper understanding. Due to the numerical definition of ϕ (Eq. 12d) Fig. 6b is supported by Table 4, which displays information on the thermal ($\bar{S}_{\Delta T}''$) and frictional ($\bar{S}_{\Delta P}''$) portions of entropy generation, as well as on ϕ for the considered Re range, at the surface roughness of $\varepsilon^* = 0.02$. It can be seen from Fig. 6b that the effects of ε^* come into sight toward the end of heating period, thus augmentations are observed in ϕ with ε^* in heating and the contrary outcome is evaluated in cooling scenarios. Computations pointed out for heating that as $\bar{S}_{\Delta T}''$ values decrease with Re and ε^* , the contrary is valid for $\bar{S}_{\Delta P}''$, where the augmentations in $\bar{S}_{\Delta P}''$ are more considerable when compared with decrease rates of $\bar{S}_{\Delta T}''$. Although the onset of the defined region varies, the mentioned character is valid for all heat flux applications. Sahin et al.'s [25] reports, for a circular heat exchanger tube, on the variations of $\bar{S}_{\Delta T}''$ and $\bar{S}_{\Delta P}''$ with ε^* , and the records of [18], for a double-sine duct, on the variations of $\bar{S}_{\Delta T}''$ and $\bar{S}_{\Delta P}''$ with Re , are completely in harmony with the present determinations. Table 4 indicates that $\bar{S}_{\Delta P}''$ values continuously increase with Re ; since $\bar{S}_{\Delta P}''$ is directly associated with velocity and mass flow rate, augmentations become more recognizable in higher Re . The decreasing character of $\bar{S}_{\Delta T}''$ in heating period with Reynolds number, results in the minimum thermal entropy

generation values of $\bar{S}_{\Delta T}'' = 0.000027 \text{ W/m}^3\text{K}$ at $Re = (Re_{cr})_{th}$, which results in the maximum ϕ data for the complete Re range. Besides, similar to the $\bar{S}_{\Delta P}''$ behavior, above the thermally critical Reynolds numbers, augmentations are also observed in $\bar{S}_{\Delta T}''$ values (Table 4). Since the increase rates are sharper than those of the frictional entropy generations, ϕ values are computed to decrease for $Re > (Re_{cr})_{th}$ (Fig. 6b, Table 4). On the other hand, computations put forward that $\bar{S}_{\Delta P}''$ values increase with heat flux both in heating and cooling cases. However, $\bar{S}_{\Delta T}''$ are evaluated to increase in heating and to decrease in cooling scenarios with surface heat flux. Moreover, the ϕ values are determined to decrease with Q and to increase with Re in heating ($Re \leq (Re_{cr})_{th}$); the corresponding data are computed to increase with heat flux and to decrease with Reynolds number in cooling ($Re \geq (Re_{cr})_{th}$). The reports of [17] for a helical coil, on the generation of ϕ with Q and Re , are completely in harmony with the current computations. Since the major portion of the total entropy generation is frictional (Table 4), the increase trends in $\bar{S}_{\Delta P}''$ with Re directly specify \bar{S}'' variations with Re (Table 3). Similar to the numerical study of [20] on low Reynolds number microchannel ($d_h = 0.61 \text{ mm}$) flows, the present computations further put forward that there exists a linear relationship among \bar{S}'' and Re on log–log basis. Such that the partial derivative of $\frac{\partial[\log \bar{S}'']}{\partial[\log Re]}$ attains the values of 2.03, 1.92 and 1.80 for $Q = 5, 50$ and 100 W/m^2 , respectively, indicating that the role of Reynolds number on entropy generation is inversely proportional to heat flux. Table 4 shows as well that, besides the augmentations in either of the $\bar{S}_{\Delta T}''$ and $\bar{S}_{\Delta P}''$ for $Re > (Re_{cr})_{th}$, $\bar{S}_{\Delta P}''$ becomes dominant to $\bar{S}_{\Delta T}''$ by occupying the major portion in the overall entropy generation (\bar{S}'').

3.2.1.4 Entropy generation aspect ratio In addition to the concepts of radial profiles, irreversibility distribution and Reynolds number–heat flux–surface roughness dependence, the aspect ratio of entropy generation (Ξ) in the

Table 4 $\bar{S}_{\Delta T}''$, $\bar{S}_{\Delta P}''$ and ϕ values for various Re and Q cases at $\varepsilon^* = 0.02$

$Q \text{ (W/m}^2\text{)}$	5			50			100		
	$\bar{S}_{\Delta T}'' \text{ (W/m}^3\text{K)}$	$\bar{S}_{\Delta P}'' \text{ (W/m}^3\text{K)}$	ϕ	$\bar{S}_{\Delta T}'' \text{ (W/m}^3\text{K)}$	$\bar{S}_{\Delta P}'' \text{ (W/m}^3\text{K)}$	ϕ	$\bar{S}_{\Delta T}'' \text{ (W/m}^3\text{K)}$	$\bar{S}_{\Delta P}'' \text{ (W/m}^3\text{K)}$	ϕ
$Re = 100$	0.0055	3.89	7.1E+02	0.4819	4.57	9.5E+00	1.56	5.38	3.4E+00
$(Re_{cr})_{th} \approx 414$	0.0000	62.43	2.3E+06						
$Re = 500$	0.0015	98.00	6.6E+04	0.4282	101.19	2.4E+02	1.91	104.89	5.5E+01
$Re = 1,000$	0.20	406.52	2.1E+03	0.0687	413.07	6.0E+03	1.05	420.43	4.0E+02
$(Re_{cr})_{th} \approx 1210$				0.0000	604.49	2.2E+07			
$Re = 1,500$	1.50	962.97	6.4E+02	0.27	973.26	3.6E+03	0.07	984.55	1.4E+04
$(Re_{cr})_{th} \approx 1635$							0.0000	1128.52	4.1E+07
$Re = 2,000$	6.30	1,778.53	2.8E+02	3.23	1,792.72	5.5E+02	1.04	1,808.59	1.7E+03

overall energy input (ψ_{inp}) of the pipe flow also needs to be considered. Defining ψ_{inp} with Eq. 18a will point out Ξ as Eq. 18b, where as the term $P_{in}\dot{Q}$ stands for the pumping energy, \dot{Q} ($=\frac{\dot{m}}{\rho}$) is the volumetric flow rate and Q_s is the total surface heat addition.

$$\Psi_{inp} = P_{in}\dot{Q} + Q_s \tag{18a}$$

$$\Xi = \frac{ST_{in}}{\Psi_{inp}} \tag{18b}$$

Figure 7 displays the variation of Ξ with various Re , ε^* and Q cases. It can be seen that, at the lowest heat flux case of $Q = 5 \text{ W/m}^2$, Ξ attains the highest rates in the complete Re range. As denoted in Table 3, entropy generation is evaluated to grow with heat flux; however the high Ξ values at low Q can be explained by the significantly low Q_s at $Q = 5 \text{ W/m}^2$ (Table 1). Figure 7 additionally implies that, in spite of the fact that S rises with ε^* , Ξ decreases with ε^* . This outcome is due to the higher P_{in} values that are applied, to attain the same Reynolds number, in the presence of augmented roughness amplitude. In other words, both the S and ψ_{inp} values grow with surface roughness but ψ_{inp} dominates. At the Reynolds number range of $Re \leq 500$, Ξ is computed to rise sharply at $Q = 5 \text{ W/m}^2$; however almost constant trends of $\Xi \approx 0.83\text{--}0.7$ ($\varepsilon^* = \varepsilon_1^* - \varepsilon_6^*$) are recognized for $Re \geq 1,250$. On the other hand, the initial increase behaviors are milder at $Q = 50$ and 100 W/m^2 , but Ξ rates are recorded to keep the augmenting styles even at the upper Reynolds number limit of 2,000. Figure 7 further covers information on the heating–cooling limits of different heat flux cases and the corresponding Ξ rates. At the thermally critical Reynolds numbers of $(Re_{cr})_{th} = 414, 1,210$ and $1,635$ the $(\Xi_{cr})_{th}$ values are evaluated as 0.462, 0.423 and 0.405, respectively. Since the major portion of entropy generation is of frictional type (Fig. 6b, Table 4), the specific Ξ values at $(Re_{cr})_{th}$ may be guiding from the

exergy analysis prospect for viscous dissipation based cooling. The indicated rates put forward that, the $(\Xi_{cr})_{th}$ values decrease with heat flux; however the rate of $\Xi \approx 0.40$ comes out to be meaningful for roughness induced laminar-transitional micropipe flows, beyond which the thermal scheme may either be of cooling type or approaching the onset.

4 Conclusions

A numerical investigation on fluid flow, heat transfer and second-law characteristics of roughness induced forced convective laminar-transitional flow inside a micropipe has been performed by the simultaneous solution of temperature dependent property continuity, momentum and energy equations. The main outcomes of the computations can be summarized as follows:

- Higher heat flux values narrows the influential Re range of ε^* on the ΔT variations, on the other hand the role of ε^* grows with Re , especially in the flows where the ΔT decreases.
- Due to viscous dissipation, there exists thermally critical Reynolds numbers; moreover high Re resulted augmentations in energy loss.
- Surface roughness is determined to accelerate transition; such that the onset Re are determined as $Re_{tra} = \sim 1,650$ ($\varepsilon^* = 0.001, \gamma = 0.132, Nu_{Re_{tra}}/Nu_{Re=1} = 1.18$), ~ 575 ($\varepsilon^* = 0.02, \gamma = 0.117, Nu_{Re_{tra}}/Nu_{Re=1} = 1.12$) and ~ 450 ($\varepsilon^* = 0.05, \gamma = 0.136, Nu_{Re_{tra}}/Nu_{Re=1} = 1.11$). These records perceive the γ and $Nu_{Re_{tra}}/Nu_{Re=1}$ ratio ranges for transition onset as $\sim 0.1\text{--}0.15$ and $\sim 1.1\text{--}1.2$.
- C_d values increase with Re and decrease with ε^* , however C_d ranges expand in higher Reynolds number cases revealing the enhanced role of ε^* on flow rate values.
- At low Reynolds numbers of $Re \leq 500$ centerline entropy values augments significantly with the increase of heat flux, however they are comparably lower than those of the wall.
- The role of ε^* on S becomes noticeable at high Re ; such that the $\bar{S}''_{\varepsilon^*=0.05}/\bar{S}''_{\varepsilon^*=0.001}$ ratio attains the values of 1.03 and 1.09 at $Re = 1,000$ and 2,000, respectively.
- As $\bar{S}''_{\Delta P}$ values continuously increase with Re , the decrease of $\bar{S}''_{\Delta T}$ in heating with Re results in the minimum $\bar{S}''_{\Delta T}$ value at $Re = (Re_{cr})_{th}$, which results in the maximum ϕ data for the complete Re range.
- ϕ values are determined to decrease with Q and to increase with Re in heating ($Re \leq (Re_{cr})_{th}$); whereas the contrary influences proceed in cooling ($Re \geq (Re_{cr})_{th}$).
- The Ξ values at $(Re_{cr})_{th}$ are meaningful from the exergy analysis prospect for viscous dissipation based cooling;

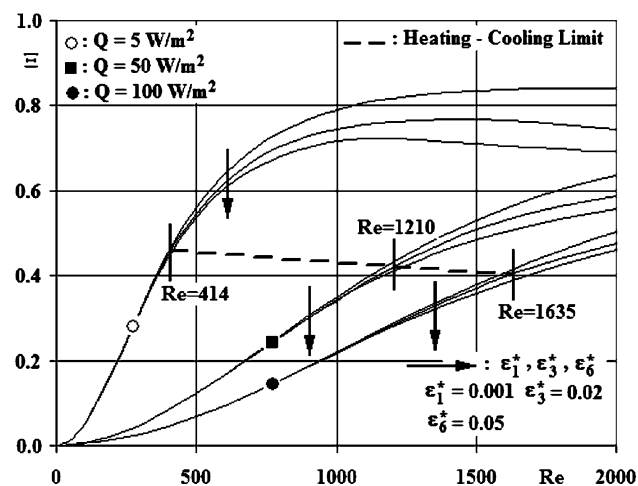


Fig. 7 Variation of Ξ with Re , ε^* and Q

moreover, the rate of $\Xi \approx 0.40$ comes out to be an indicator for cooling onset.

References

- Granovskii M, Dincer I, Rosen MA (2006) Application of oxygen ion-conductive membranes for simultaneous electricity and hydrogen generation. *Chem Eng J* 120:193–202
- Lin WW, Lee DJ (1998) Second-law analysis on wavy plate fin-and-tube heat exchangers. *J Heat Trans ASME Trans* 120:797–801
- Obot NT (2002) Toward a better understanding of friction and heat/mass transfer in microchannels—a literature review. *Microscale Thermophys Eng* 6:155–173
- Kandlikar SG, Joshi S, Tian S (2003) Effect of surface roughness on heat transfer and fluid flow characteristics at low Reynolds numbers in small diameter tubes. *Heat Trans Eng* 24:4–16
- Wen MY, Jang KJ, Yang CC (2003) Augmented heat transfer and pressure drop of strip-type inserts in the small tubes. *Heat Mass Trans* 40:133–141
- Guo ZY, Li ZX (2003) Size effect on microscale single-phase flow and heat transfer. *Int J Heat Mass Trans* 46:149–159
- Koo J, Kleinstreuer C (2004) Viscous dissipation effects in microtubes and microchannels. *Int J Heat Mass Trans* 47:3159–3169
- Morini GL (2005) Viscous heating in liquid flows in microchannels. *Int J Heat Mass Trans* 48:3637–3647
- Celata GP, Cumo M, McPhail S, Zummo G (2006) Characterization of fluid dynamic behaviour and channel wall effects in microtube. *Int J Heat Fluid Flow* 27:135–143
- Celata GP, Morini GL, Marconi V, McPhail SJ, Zummo G (2006) Using viscous heating to determine the friction factor in microchannels—An experimental validation. *Exp Thermal Fluid Sci* 30:725–731
- Wu HY, Cheng P (2003) An experimental study of convective heat transfer in silicon microchannels with different surface conditions. *Int J Heat Mass Trans* 46:2547–2556
- Phares DJ, Smedley GT, Zhou J (2005) Laminar flow resistance in short microtubes. *Int J Heat Fluid Flow* 26:506–512
- Vicente PG, Garcia A, Viedma A (2002) Experimental study of mixed convection and pressure drop in helically dimpled tubes for laminar and transition flow. *Int J Heat Mass Trans* 45:5091–5105
- Engin T, Dogruer U, Evrensel C, Heavin S, Gordaninejad F (2004) Effect of wall roughness on laminar flow of Bingham plastic fluids through microtubes. *J Fluids Eng ASME Trans* 126:880–883
- Sahin AZ (1998) Second-law analysis of laminar viscous flow through a duct subjected to constant wall temperature. *J Heat Trans ASME Trans* 120:77–83
- Zimparov V (2002) Energy conservation through heat transfer enhancement techniques. *Int J Energy Res* 26:675–696
- Ko TH (2006) Numerical investigation of laminar forced convection and entropy generation in a helical coil with constant wall heat flux. *Num Heat Trans Part A* 49:257–278
- Ko TH (2006) Numerical analysis of entropy generation and optimal Reynolds number for developing laminar forced convection in double-sine ducts with various aspect ratios. *Int J Heat Mass Trans* 49:718–726
- Ratts EB, Raut AG (2004) Entropy generation minimization of fully developed internal flow with constant heat flux. *J Heat Trans ASME Trans* 126:656–659
- Richardson DH, Sekulic DP, Campo A (2000) Low Reynolds number flow inside straight micro channels with irregular cross sections. *Heat Mass Trans* 36:187–193
- Zimparov V (2000) Extended performance evaluation criteria for enhanced heat transfer surfaces: heat transfer through ducts with constant wall temperature. *Int J Heat Mass Trans* 43:3137–3155
- Rakshit D, Balaji C (2005) Thermodynamic optimization of conjugate convection from a finned channel using genetic algorithms. *Heat Mass Trans* 41:535–544
- Ozalp AA (2006) A computational study to predict the combined effects of surface roughness and heat flux conditions on converging-nozzle flows. *Trans Can Soc Mech Eng* 29:67–80
- Ozalp AA (2007) Parallel effects of acceleration and surface heating on compressible flow: simulation of an aerospace propulsion nozzle with a medium amount of surface wear. *Strojinski Vestnik J Mech Eng* 53:3–12
- Sahin AZ, Zubair SM, Al-Garni AZ, Kahraman R (2000) Effect of fouling on operational cost in pipe flow due to entropy generation. *Energy Conv Manag* 41:1485–1496
- Cao BY, Chen M, Guo ZY (2006) Effect of surface roughness on gas flow in microchannels by molecular dynamics simulation. *Int J Eng Sci* 44:927–937
- Wang H, Wang Y, Zhang J (2005) Influence of ribbon structure rough wall on the microscale Poiseuille flow. *J Fluids Eng ASME Trans* 127:1140–1145
- Sheikh AK, Zubair SM, Younas M, Budair MO (2001) Statistical aspects of fouling processes. *Proc Instn Mech Engrs Part E* 215:331–354
- Incropera FP, DeWitt DP (2001) Fundamentals of heat and mass transfer. Wiley, New York
- Wu JS, Tseng KC (2001) Analysis of micro-scale gas flows with pressure boundaries using direct simulation Monte Carlo method. *Comput Fluids* 30:711–735
- White FM (1988) Fluid mechanics. McGraw-Hill, Singapore
- Wu P, Little WA (1983) Measurement of friction factors for the flow of gases in very fine channels used for microminiature Joule–Thompson refrigerators. *Cryogenics* 23:273–277
- Sahin B, Ceyhan H (1996) Numerical and experimental analysis of laminar flow through square-edged orifice with variable thickness. *Trans Inst Meas Control* 178:166–174